Diese Arbeit wurde vorgelegt am
Lehr- und Forschungsgebiet Theorie der hybriden Systeme

Entwicklung eines Simulationsmodells zur Optimierung von Ausrichtung, Neigung und Reihenabständen in Photovoltaik-Freiflächenparks

Development of a Simulation Model for Optimizing Orientation, Tilt and Row Spacing in Ground-Mounted Solar Photovoltaic Parks

Bachelorarbeit
Informatik

Dezember 2025

Vorgelegt von
Presented by
Maximilian Dömel
Matrikelnummer: 444825
maximilian.doemel@rwth-aachen.de

Erstprüfer
First examiner
Prof. Dr. Dr. h.c. Erika Ábrahám
Lehr- und Forschungsgebiet: Theorie Hybrider Systeme
RWTH Aachen University

Zweitprüfer
Second examiner
Prof. Dr. rer. nat. Jürgen Giesl
Lehr- und Forschungsgebiet: Programmiersprachen und Verifikation
RWTH Aachen University

Betreuer
Supervisor
Dr. rer. nat. Pascal Richter
Lehr- und Forschungsgebiet: Theorie Hybrider Systeme
RWTH Aachen University

Contents

List of Symbols

a	modified nonideality factor [V]
a_{ref}	reference modified nonideality factor [V]
a, b	parameters depending on module type and mounting configuration of the module (see Tab. 3) [unitless]
a_1, a_2	altitude dependent coefficients (see Eq. 9 and Eq. 10) [unitless]
Adjust	adjustment factor [unitless]
altitude	altitude [m]
AM	air mass [unitless]
$\mathrm{AM_a}$	absolute airmass [unitless]
$\mathrm{AM_r}$	relative airmass at sea level [unitless]
C_0	parameter defining the curvature of the relationship between AC power and DC power [unitless]
C_1, C_2, C_3	empirical parameters describing linear variations [1/V]
D	inter-row gap [m]
D'	inter-row gap to the middle of the posterior PV module row [m]
D_{N}	inter-row gap for N PV module rows [m]
DHI	diffuse horizontal irradiance [$\mathrm{W/m^2}$]
DNI	direct normal irradiance [$\mathrm{W/m^2}$]
E_{g}	bandgap energy eV
$E_{\mathrm{g,ref}}$	reference bandgap energy $\approx 1.121\,\mathrm{eV}$ (for silicon)
f_{h1}, f_{h2}	coefficients relating the station's altitude with the altitude of the
F_1	circumsolar brightness coefficient [unitless]
F_2	horizon brightness coefficient [unitless]
F_{ground}	ground view factor [unitless]
	atmospheric interactions (see Eq. 7 and Eq. 11)
F_{sky}	sky view factor [unitless]
GHI	global horizontal irradiance [$\mathrm{W/m^2}$]
h	height difference between the PV module's highest and lowest edges [m]
I	output current [A]
I_0	diode reverse saturation current [A]
$I_{0,\mathrm{ref}}$	reference diode saturation current [A]
I_{D}	voltage-dependent current lost to recombination [A]
I_{ext}	extraterrestrial irradiance [$\mathrm{W/m^2}$]
I_{L}	light-generated current [A]
$I_{\mathrm{L,ref}}$	reference light-generated current [A]
I_{sh}	shunt current [A]

k	Boltzmann constant = $1.3807 \cdot 10^{-23}$ J/K
K	glazing extinction coefficient ≈ 4 1/m (for "water white" glass)
$K_{\tau\alpha}$	incidence angle modifier [unitless]
l	length of the area of the solar park [m]
L	glazing thickness ≈ 2 mm (typical value)
n_{air}	refractive index of air ≈ 1
n_{glass}	refractive index of glass ≈ 1.526
N	number of solar panel rows [unitless]
N_{max}	maximum number of PV module rows [unitless]
P	atmospheric pressure [Pa]
P_{ac}	AC output power [W]
P_{aco}	AC power rating [W]
P_{dc}	DC input power [W]
P_{dco}	DC power input at reference voltage resulting in P_{aco} [W]
POA	plane-of-array irradiance [W/m^2]
$\text{POA}_{\text{diffuse}}$	diffuse component of POA irradiance [W/m^2]
$\text{POA}_{\text{direct}}$	direct component of POA irradiance [W/m^2]
POA_{eff}	effective POA irradiance [W/m^2]
$\text{POA}_{\text{ground}}$	ground component of POA irradiance [W/m^2]
POA_{reg}	unshaded annual POA irradiance [W h]
$\text{POA}_{\text{shaded,D}_\text{N}}$	annual POA irradiance with shading losses for inter-row gap D_N [W h]
POA_{tot}	total annual POA irradiance [W h]
R_{s}	series resistance [Ω]
R_{sh}	shunt resistance [Ω]
T_{a}	ambient air temperature [°C]
T_{c}	cell temperature [°C]
T_{LK}	Linke turbidity coefficient [unitless]
T_{m}	module back-surface temperature [°C]
T_{NOCT}	nominal operating cell temperature [°C]
V	output voltage [V]
w	PV module's width [m]
w'	PV module's projected width [m]
WS	wind speed [m/s]

α_{full}	shallowest solar elevation angle without self-shading [°]
α_{half}	shallowest solar elevation angle with 50 % self-shading [°]
$\alpha_{\text{sc,ref}}$	reference temperature coefficient of short-circuit current [unitless]
β	PV modules's tilt angle [°]
θ_{diffuse}	diffuse effective angle [°]
θ_{ground}	ground effective angle [°]
θ_{i}	angle of incidence [°]
θ_{r}	angle of refraction [°]
θ_{z}	solar zenith angle [°]
ρ	albedo [unitless]
$\tau\alpha(\theta_{\text{i}})$	transmittance-absorbtance product for incidence angle θ_{i} [unitless]

1 Introduction

This thesis introduces a two-step optimization framework, which calculates the optimal tilt and azimuth angles of a photovoltaic (PV) module based on annual plane-of-array irradiance for a given location. Additionally, it proposes a self-shading model, which is then used to determine the optimal inter-row gap for a given area of the PV park based on the levelized cost of electricity. The different underlying models are introduced and compared, and the results of the optimization are validated.

1.1 Motivation

Photovoltaik (PV) parks play a critical role in Germany's energy transition within the broader framework of the European Union's goal of achieving carbon neutrality by 2050. Ground-mounted PV systems, in particular, are central to scaling up solar capacity because of their ability to contribute significantly to national electricity generation while reducing dependence on conventional energy sources. Recent data from Germany's Federal Statistical Office (Destatis) [3] underlines this importance: in the first half of 2025, electricity generation from PV increased by 27.9% compared to the same period in 2024, reaching 39.3 billion kilowatt-hours. With a share of 17.8% of total domestic electricity production, PV became the third most important energy source, surpassing natural gas. This significant growth is attributed both to the expansion of installed capacity and unusually high sunshine duration, highlighting PV's rapidly growing role in Germany's energy mix.

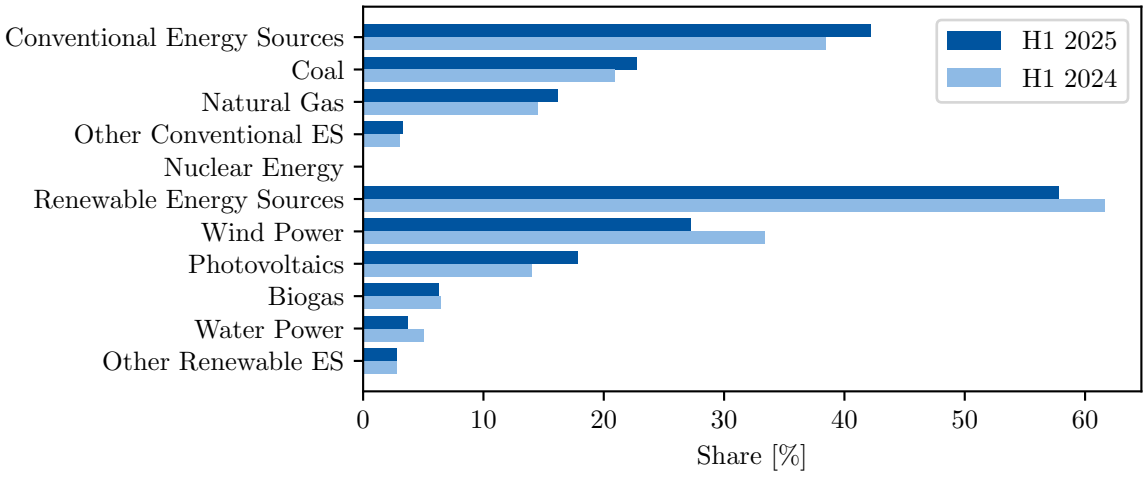

Figure 1: Electricity feed-in from renewable and conventional energy sources [4].

The motivation for developing a simulation model to optimize orientation, tilt, and row spacing in ground-mounted PV parks lies in the growing demand for efficient, cost-effective and sustainable solar energy systems. While PV is now one of the fastest-growing renewable energy technologies, maximizing its performance requires careful consideration of both technical and economic parameters.

Ground-mounted PV parks are highly sensitive to design factors such as the azimuth and tilt angle, as well as the row spacing, which directly influence energy yield, land-use efficiency, shading losses, and overall financial viability. Conventional design practices often rely on statistical assumptions or generalized guidelines that fail to account for site-specific conditions such as latitude, local climate, and seasonal solar angles. This can result in suboptimal layouts, reduced energy production, and higher project costs.

The proposed simulation model provides a systematic framework to evaluate alternative configurations before implementation. In addition to integrating solar geometry, shading analysis, and energy yield estimation, the model is also capable of calculating the levelized cost of electricity (LCOE) for a planned PV park. This makes it possible to assess not only technical efficiency but also economic profitability, turning the model into a comprehensive design and decision-support tool.

Ultimately, this research addresses the urgent need for precise, data-driven tools to strengthen the efficiency, reliability, and profitability of solar PV projects. Given the accelerating role of PV in Germany's power supply, as shown by its rapid capacity growth and rising contribution to domestic electricity generation, optimizing PV park design is central not only to the country's energy transition but also to advancing scalable, cost-optimized renewable energy solutions in line with the EU's carbon neutrality pathway.

1.2 Outline

First, we introduce which data is needed to perform the simulation of a PV system. Focusing on solar radiation, as well as parameters of PV modules and inverters, we cover how they originate, what their relevance in the simulation is, which data is needed, and how to source them.

Next, we introduce underlying models used by our optimization. Here, we cover why the model is used and how its results are calculated. If necessary, we compare models that simulate the same effect.

Then, we start with the first part of our two-step optimization, the optimization of the module's orientation. Therefore, we use and compare several models introduced before, as well as different sources of irradiance. Afterwards, we draw a conclusion, which combination of models and irradiance data sources is most accurate by comparing them to a validation set and which algorithm is most performant without reducing the accuracy of the result.

As for the second step, we introduce the self-shading model and its significance on the optimal inter-row gap. In order to determine the optimal inter-row gap, we optimize after three evolving objective functions which lead to the optimization after the minimal levelized cost of electricity. The accuracy of this model is then compared against a recent PV park in Germany in order to evaluate its accuracy.

In the end, we draw a conclusion, highlight the results of this thesis, and provide an outlook on the future work.

2 Model Inputs

In order to simulate the performance of a PV system, data about the system and its environment is necessary. This includes specifications on the components used by the system, such as the PV module and the inverter. Additionally, data about the solar radiation at the specific location of the PV system is needed, like the intensity of solar radiation throughout the year.

2.1 Solar Radiation

Following Wesselak and Voswinckel [21], the source of the solar radiation used by the photovoltaic effect to produce energy in solar cells lies at the Sun's core. There, during an atomic chain reaction, hydrogen cores fuse to helium cores, releasing a fraction of the excess energy in form of photons. This causes the Sun's surface to emit electromagnetic radiation, whose intensity decreases quadratically with the distance from the Sun. At Earth's atmosphere, this radiation is described by the solar constant $I_{SC} = 1366.1\,\mathrm{W/m^2}$. The matter of the atmosphere then interacts with the radiation in the form of reflections and scatterings. This leads to 28 % of the radiation being reflected back into space and 25 % being absorbed, mainly by steam and ozone. 22 % of the radiation reaching the atmosphere passes it without interactions and, therefore, reaches Earth's surface without reflections and scatterings, the so-called direct radiation, while 25 % reach the surface after such interactions, the so-called diffuse radiation. These proportions are taken from the averaged radiation balance of the Earth. For a specific location, the ratio between direct and diffuse radiation differs based on weather and the Sun's position. If the weather is clear, the percentage of the direct radiation rises, while the percentage of the diffuse radiation lowers. During cloudy weather, the opposite is the case. Similarly, when the Sun is lower in the sky, the path of radiation through the atmosphere is longer. Therefore, the portion of diffuse radiation rises and the portion of direct radiation lowers.

To simulate the power output of a PV system, accurate measurements or projections of the radiation data for the specific location of the PV system are crucial. That is why performance simulations of a PV system require this data in a structured form. Usually, the radiation components needed for such a simulation are called direct normal irradiance (DNI), diffuse horizontal irradiance (DHI), and global horizontal irradiance (GHI). Whilst DNI measures the direct radiation perpendicularly to the Sun's direction, DHI is the diffuse radiation from the atmosphere measured on a horizontal surface collecting radiation from all points of the sky. In addition to both of these components, the third one, GHI, is the total solar radiation on a horizontal surface. It is the sum of the DNI with respect to the solar zenith angle and the DHI as seen in Eq. 1. PV system performance simulations typically expect these three components as time series aggregated to fixed intervals, e.g. hourly, daily, or monthly. You can obtain this data either through simulation of a radiation model or by downloading it from a radiation database.

$$\mathrm{GHI} = \mathrm{DHI} + \mathrm{DNI} \cdot \cos\theta_\mathrm{z} \tag{1}$$

with

GHI	global horizontal irradiance [W/m^2]
DHI	diffuse horizontal irradiance [W/m^2]
DNI	direct normal irradiance [W/m^2]
θ_z	solar zenith angle [°]

2.1.1 Simulated Radiation Data

As for simulating radiation data, there are multiple viable models which can be categorized into two groups: clear-sky models or all-sky models. As the name suggests, clear-sky models are subject to the restriction that there are cloud-free conditions at all times. All-sky models, on the other hand, take account of weather circumstances, such as cloudy skies. Therefore, they need access to measurements of weather stations or geostationary satellites.

As for the clear-sky models, the most widely adopted model in practice is the Ineichen model. Its advantages are competitive performance with other models whilst being simpler, thus requiring less computational complexity. The model computes clear-sky DNI, GHI, and DHI using solar geometry, absolute airmass, Linke turbidity, altitude, and extraterrestrial irradiance. The absolute airmass can be derived from the atmospheric pressure and the relative airmass (Eq. 2).

$$\mathrm{AM_a} = \mathrm{AM_r} \cdot \frac{P}{101\,325\,\mathrm{Pa}} \tag{2}$$

with

$\mathrm{AM_a}$	absolute airmass [unitless]
$\mathrm{AM_r}$	relative airmass at sea level [unitless]
P	atmospheric pressure [Pa]
101 325 Pa	standard sea-level pressure

The relative airmass can be calculated using the numerical constants from Kasten and Young [8], as well as the solar zenith angle (Eq. 3).

$$\mathrm{AM}_r = \frac{1}{\cos(z) + 0.505\,72 \cdot (96.079\,95 - \theta_\mathrm{z})^{-1.6364}} \tag{3}$$

Since the extraterrestrial irradiance varies slightly throughout the year, it is calculated using a Fourier series-based model created by Spencer [20], shown in Eq. 4.

$$\begin{aligned} I_\mathrm{ext} = I_\mathrm{SC}[&1.000\,11 + 0.034\,221 \cdot \cos(x) + 0.001\,28 \cdot \sin(x) \\ &-0.000\,719 \cdot \cos(2x) + 0.000\,077 \cdot \sin(2x)] \end{aligned} \tag{4}$$

with

I_ext	extraterrestrial irradiance [W/m^2]

The Linke turbidity factor can be derived from historical monthly averages, either by using the monthly value or an interpolated value which smoothes the transition between months. This leads to the equations of the clear-sky DNI (Eq. 5)

$$\mathrm{DNI} = b \cdot I_{\mathrm{ext}} \cdot \exp\left(-0.09 \cdot \mathrm{AM_a} \cdot (T_{\mathrm{LK}} - 1)\right) \tag{5}$$

$$b = 0.664 + \frac{0.163}{f_{\mathrm{h1}}} \tag{6}$$

$$f_{h1} = \exp\left(-\frac{\mathrm{altitude}}{8000}\right) \tag{7}$$

with

altitude	altitude [m]
T_{LK}	Linke turbidity coefficient [unitless]

and GHI (Eq. 8)

$$\mathrm{GHI} = a_1 \cdot I_{\mathrm{ext}} \cdot \sin(h) \cdot \exp\left(-a_2 \cdot \mathrm{AM_a} \cdot (f_{\mathrm{h1}} + f_{\mathrm{h2}} - (T_{\mathrm{L}} - 1)\right) \tag{8}$$

$$a_1 = 5.09 \cdot 10^{-5} \cdot \mathrm{altitude} + 0.868 \tag{9}$$

$$a_2 = 3.92 \cdot 10^{-5} \cdot \mathrm{altitude} + 0.0387 \tag{10}$$

$$f_{\mathrm{h2}} = \exp\left(-\frac{\mathrm{altitude}}{1250}\right) \tag{11}$$

with

$\mathrm{GHI_I}$	global horizontal irradiance [$\mathrm{W/m^2}$]
a_1, a_2	altitude dependent coefficients (see Eq. 9 and Eq. 10)
$\mathrm{AM_a}$	absolute airmass [unitless]
f_{h1}, f_{h2}	coefficients relating the station's altitude with the altitude of the atmospheric interactions (see Eq. 7 and Eq. 11)

according to the Ineichen model [7]. Lastly, the DHI can be derived by rearranging Equation 1 for DHI as in Eq. 12.

$$\mathrm{DHI} = \mathrm{GHI} - \mathrm{DNI} \cdot \cos\theta_{\mathrm{z}} \tag{12}$$

Since all-sky models need even more parameters to calculate GHI, DNI, and DHI, such as cloud parameters (e.g. cloud coverage, optical thickness, type), we focus on retrieving those values from solar radiation databases.

2.1.2 Solar Radiation Databases

Following pvlib python [17], solar radiation databases differ primarily in the way data is sourced. First off, there is weather data sourced from ground station measurements. Under the right conditions, these are the highest quality source of weather information. On the downside, coverage of such weather stations is limited. Alternatively, there are mathematical simulations for weather systems using numerical weather prediction (NWP). The benefit of these models is global coverage, however, by sacrificing spatial and temporal resolution and data quality. Additionally, many of those models are not optimised for solar irradiance for PV simulations. Lastly, there is data sourced from the processing of satellite imagery. Irradiance estimates are calculated using simulations of solar irradiance models after identification and classification of clouds on the satellites' images. The data quality of these estimates is not as good as the one of ground stations, but it is much higher compared to NWP. Due to the high satellite coverage, data availability is significantly higher than that of ground stations. In contrast to NWP, weather data from satellites is generally optimised to estimate solar irradiance for PV applications. Concluding this, measurements from ground stations should be preferred, directly followed by data derived from satellite imagery, and only if both of these sources are unavailable, NWP should be considered. There are multiple sources available, that differ in source type, temporal resolution, spatial coverage, provided components, format, and licensing, amongst others. In the following, we will compare different providers.

Starting off with the Deutscher Wetterdienst (DWD), Germany's national meteorological service, it provides ground station measurements of 95 stations across Germany. These measurements are available in ten-minute intervals with historical data depending on the station. Because it is based off ground stations, spatial coverage depends on the location of them. The data includes measurements of DNI and GHI, as well as a quality level and is available in a textual, CSV-like form under the Creative Commons (CC) BY 4.0 license from their Climate Data Center.

Next, there is the Photovoltaic Geographical Information System (PVGIS) [16], operated by the European Commission. They maintain multiple solar radiation databases. On the one hand, there is the satellite-based PVGIS-SARAH3 database with up to hourly time-series data ranging from 2005 to 2023. PVGIS-SARAH3 covers Europe, Central Asia, Africa, and parts of South America with a spatial resolution of 5 km. For the rest of the world, PVGIS-ERA5 is a reanalysis database with the same temporal resolution, but only with a spatial resolution of roughly 25 km. The time-series data of both databases contain direct, diffuse, and reflected irradiance relative to an inclined plane, Sun height, air temperature, and wind speed. Since PVGIS is tailored towards PV systems modelling, there is an option to specify the mounting type (fixed, horizontal/vertical/both axis tracked), tilt, and azimuth angles of the module and PV power parameters. There is even an option to optimize tilt and azimuth angles with regard to the given input parameters. Additionally, there is the option to take terrain shadows into account for the radiation components using a calculated horizon or your own horizon data. When using the calculated horizon, data of the ground elevation

with a resolution of approximately 90 m is used to calculate shading effects from local hills or mountains. For a higher level of detail, when nearby objects like houses or trees should be considered as well, you can upload your own horizon information.

Another alternative is the Copernicus Atmosphere Monitoring Service (CAMS). Their solar radiation services combine ground station measurements, numerical weather prediction, and data derived from satellite imagery to provide historical time-series data with a temporal resolution of 1 min and a time coverage from 2004 up until now. Geographical coverage includes Europe, Africa, the Middle East, the Atlantic Ocean, Brazil, the east of Asia, Oceania, and Australia. The data includes GHI, DHI, and DNI for an all-sky and a clear-sky model in either ASCII (CSV) or NetCDF format. It is licensed under CC BY 4.0 and can be accessed through their Atmosphere Data Store.

Commercial solar radiation data providers like SolarAnywhere, Solcast, and Solargis offer high-quality datasets derived from satellite imagery, NWP models, and ground station measurements. However, they are not considered in this study, since our focus lies on publicly available solar radiation resources exclusively.

2.1.3 Selected Data Sources

As for the solar radiation input data sources, time-series data from both the Ineichen clear-sky model and the PVGIS-ERA5 database are included. On the one hand, the Ineichen clear-sky model is known for its rigorous physical basis in calculating cloud-free irradiance. On the other hand, the PVGIS-ERA5 database provides comprehensive all-sky irradiance data using satellite imagery. These two data sources will be directly compared to evaluate their performance in representing solar radiation accurately. The outcome of this comparison will determine which data source is used for the subsequent simulations.

2.2 PV Modules and Inverters

The conversion of solar radiation energy to electric energy is a two-step process. First of all, the PV module collects the radiation generating direct current (DC) energy. Besides the intensity of the radiation, the DC output depends on various characteristics of the used PV module, such as the nominal maximum power and temperature coefficients. Since the power grid utilizes alternating current (AC) rather than DC to transmit the electric energy more efficiently over long distances, we must convert the DC output to AC in a second step using an inverter. During this conversion, electric energy is lost due to heat dissipation and switching losses. This also depends on the characteristics of the used inverter, like the weighted efficiency.

2.2.1 PV Modules

Following Wesselak and Voswinckel [21], a PV module is a composition of PV cells. These PV cells are made of semiconductor material, which is most commonly built

from a p-n junction of doped silicon. The n-layer is doped by adding phosphorus atoms to the silicon atom lattice to obtain additional electrons, while the p-layer is doped by adding boron atoms to obtain additional holes. Where these two layers meet, the excess electrons of the n-layer fill up the holes of the p-layer, creating a depletion area with an electric field pointing from the n-layer to the p-layer. When a photon hits the surface of the n-layer and gets absorbed by the semiconductor, it excites an electron from the valence band to the conduction band, which creates an electron-hole pair. The electric field of the p-n junction then separates these charges, pushing the electron towards the n-layer and the hole towards the p-layer. The electrons on the top of the n-layer build up a voltage, so that, if that layer is connected to the bottom of the p-layer conductively using suitable contacts, a current flow is established. The level of voltage and current depends on light intensity, the cell's surface area, temperature, and the material's efficiency.

Parameter	**Value**
Technology	Mono-c-Si
Bifacial	✓
Building-integrated PV (BIPV)	✗
Peak power at standard test conditions (STC)	551.04 W
Peak power at PVUSA test conditions (PTC)	506.9 W
Module length	2.278 m
Module width	1.134 m
Module area (A_c)	2.51 m^2
Cells in series (N_s)	72
Short-circuit current ($I_{sc,ref}$)	13.99 A
Open-circuit voltage ($V_{oc,ref}$)	49.8 V
Current at maximum power point ($I_{mp,ref}$)	13.12 A
Voltage at maximum power point ($V_{mp,ref}$)	42.0 V
Temperature coefficient of short-circuit current (α_{sc})	0.006 295 A/°C
Temperature coefficient of open-circuit voltage (β_{oc})	−0.132 468 V/°C
Nominal operating cell temperature (T_{NOCT})	48.7 °C
Modified diode ideality factor at reference conditions (a_{ref})	1.885 45
Light-generated current ($I_{L,ref}$)	14.0029 A
Diode saturation current ($I_{0,ref}$)	0.0 A
Series resistance (R_s)	0.146 344 Ω
Shunt resistance ($R_{sh,ref}$)	158.173 Ω
Adjustment factor (Adjust)	12.4951 %
Temperature coefficient of maximum power point (γ_{pmp})	−0.354 %/°C

Table 1: Parameters of the LONGi LR5-72HBD-550M module sourced from the CEC module database [13].

Using PV module databases, like the ones from the California Energy Commission (CEC) or Sandia, these parameters can be retrieved for a specific module. In this

thesis, we chose to use the LR5-72HBD-550M panel by LONGi Green Energy Co. Ltd., since it is a typical module used in recent utility-scale PV parks, such as the one in Langenenslingen-Wilfingen in Baden-Wuerttemberg, Germany. Its entry in the CEC database has the parameters listed in Table 1.

2.2.2 Inverters

Since we are optimizing grid-connected PV parks and the power grid operates at AC current, we need to convert the DC current produced by the PV modules to AC current. During this conversion, electric energy is lost, depending on several parameters of the chosen inverter. As with the PV modules, these parameters can be sourced from databases like CEC or Sandia. The entry of the inverter we chose for the optimization, the ABB MICRO-0.25-I-OUTD-US-208 (208V), is shown in Table 2.

Parameter	Value
Nominal AC output voltage (V_{ac})	208 V
DC power required to start the inversion process (P_{so})	2.089 607 W
AC power rating (P_{aco})	250.0 W
DC power input at reference voltage resulting in P_{aco} (P_{dco})	259.588 593 W
Reference voltage for P_{so} and P_{aco} (V_{dco})	40.0 V
Parameter defining the curvature of the relationship between AC power and DC power (C_0)	−0.000 041
Empirical coefficient allowing P_{dco} to vary linearly with DC voltage input (C_1)	−0.000 091/V
Empirical coefficient allowing P_{so} to vary linearly with DC voltage input (C_2)	0.000 494/V
Empirical coefficient allowing C_0 to vary linearly with DC voltage input (C_3)	−0.013 171/V
Night tare (P_{nt})	0.075 W
Maximum allowable DC input voltage ($V_{\text{dc,max}}$)	50.0 V
Maximum allowable DC input current ($I_{\text{dc,max}}$)	6.648 971 5 A
Lower limit of the maximum power point voltage window (MPP_{low})	30.0 V
Upper limit of the maximum power point voltage window (MPP_{high})	50.0 V

Table 2: Parameters of the ABB MICRO-0.25-I-OUTD-US-208 (208V) sourced from the CEC inverter database [13].

3 Simulation of a PV System's Performance

In order to optimize the orientation and inter-row gap of a PV park, we make use of several well-established simulation models. First off, for the optimization of the azimuth and tilt angles, we use the solar position and transposition models to calculate the plane-of-array (POA) irradiance. Based on the results, we optimize the inter-row gap of the module rows using a model for the cell temperature, the incidence angle modifier (IAM), the photovoltaic effect, and the inverter.

3.1 Solar Position Model

The position of the Sun on the horizon is crucial for determining the irradiance which actually lands on the tilted module plane. For a specified location and date, it is given by two angles, the zenith angle and the azimuth angle. The zenith angle is the angle between the Sun's rays and the local vertical, whereas the azimuth angle specifies the compass direction of the Sun.

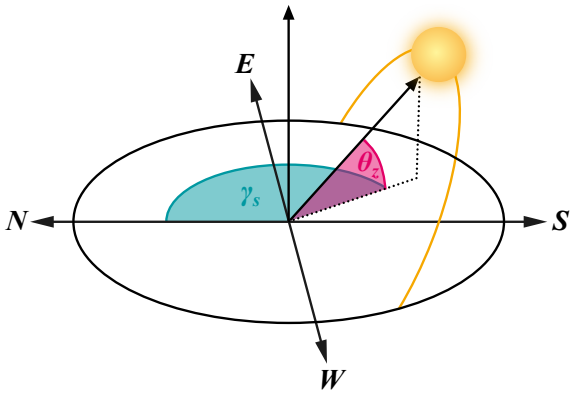

Figure 2: Sun's position described by solar azimuth angle γ_s and solar zenith angle θ_z.

To calculate these angles, we make use of the NREL Solar Position Algorithm [19], which calculates the angles in the period from the year 2001 BCE to 6000 CE with uncertainties of +/- 0.0003° based on date, time, and location on Earth.

3.2 Transposition Model

A solar transposition model is used to convert the solar irradiance components from a horizontal or normal plane to the plane-of-array (POA) on a module of any given tilt. There are multiple models on how to calculate the POA irradiance. In the following, we introduce two popular ones: the isotropic model, a simple and easy-to-calculate model, and the Perez model, a more complex and more accurate model.

3.2.1 Isotropic Model

The isotropic transposition model [12] is based on the assumption that diffuse radiation is uniform across the entire sky dome. This means it assumes the scattered light coming from the horizon has exactly the same intensity as the scattered light coming from the area around the Sun. That reduces calculating the irradiance on a tilted plane to a simple geometric problem. Depending on the tilt angle of the plane, the diffuse radiation is multiplied with a sky view factor (Eq. 13). If the plane is horizontal, the factor is one, meaning the plane receives all of the diffuse irradiance. If it is vertical, the factor is 0.5, meaning it sees exactly half of the sky dome, resulting in half of the diffuse irradiance.

$$F_{\text{sky}} = \frac{1 + \cos\beta}{2} \tag{13}$$

with

F_{sky} sky view factor [unitless]
β tilt angle of the plane [°]

Similarly, this concept is applied to ground reflections. Since the ground reflects both diffuse and direct irradiance, the reflection's irradiance is based on the GHI multiplied by the reflectivity factor of the ground (albedo). Instead of the sky view factor, a ground view factor (Eq. 14) is considered. If the plane is horizontal, the factor is zero, meaning the plane receives none of the ground-reflected irradiance. If it is vertical, the factor is 0.5, meaning it sees half of the ground, resulting in half of the ground-reflected irradiance.

$$F_{\text{ground}} = \frac{1 - \cos\beta}{2} \tag{14}$$

with

F_{ground} ground view factor [unitless]

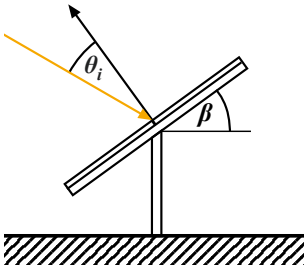

Figure 3: Angle of incidence θ_{i} on a tilted plane.

Since the plane is not always perpendicular to the Sun's rays, the DNI must be scaled with an obliquity factor. Therefore, we multiply it with the cosine of the angle of incidence (Fig. 3). The factor is one if the angle of incidence is 0 °, meaning the tilt angle of the PV module is the same as the solar zenith angle. Therefore, the plane

is perpendicular to the Sun's rays and the DNI applies. If the angle of incidence is greater, the factor gets smaller. Since the same radiant power is then spread over a larger actual area, the DNI must be scaled down. Finally, the POA irradiance according to the isotropic model is the sum of the DNI scaled by the angle of incidence, the DHI scaled by the sky view factor, and the GHI scaled by the albedo and the ground view factor (Eq. 15).

$$\mathrm{POA} = \mathrm{DNI} \cdot \cos\left(\theta_\mathrm{i}\right) + \mathrm{DHI} \cdot F_\mathrm{sky} + \mathrm{GHI} \cdot \rho \cdot F_\mathrm{ground} \tag{15}$$

with

POA	plane-of-array irradiance [W/m^2]
DNI	direct normal irradiance [W/m^2]
θ_i	angle of incidence [°]
DHI	diffuse horizontal irradiance [W/m^2]
GHI	global horizontal irradiance [W/m^2]
ρ	albedo [unitless]

3.2.2 Perez Model

The Perez transposition model [12] is a more sophisticated method compared to the isotropic model. It is an anisotropic model, meaning it accounts for the fact that the sky is not uniformly bright. Therefore, the diffuse irradiance gets split into three distinct parts to better model reality. First off, the background sky brightness is assumed to be uniform, just like the isotropic model. Then there is the circumsolar region, the intense brightening around the Sun's disk, which is treated almost like the direct beam. Lastly, there is the horizon band, which refers to the brightening often seen near the horizon, especially in clear skies. To account for the circumsolar region and the horizon band, two empirically determined factors are introduced, the circumsolar brightness coefficient and the horizon brightness coefficient. After implementing this into the equation of the isotropic transposition model (Eq. 15) using its sky (Eq. 13) and ground view factor (Eq. 14), we receive the equation for the Perez transposition model (Eq. 18).

$$a = \max\left(0\,^\circ, \cos\theta_\mathrm{i}\right) \tag{16}$$

$$b = \max\left(\cos 85\,^\circ, \cos\theta_\mathrm{z}\right) \tag{17}$$

$$\mathrm{POA} = \mathrm{DNI}\cdot\cos\left(\theta_\mathrm{i}\right) + \mathrm{DHI}\cdot\left[\left(1 - F_1\right)\cdot F_\mathrm{sky} + F_1 \cdot \frac{a}{b} + F_2 \cdot \sin\beta\right] + \mathrm{GHI}\cdot\rho\cdot F_\mathrm{ground} \tag{18}$$

with

θ_z	solar zenith angle [°]
F_1	circumsolar brightness coefficient [unitless]
F_sky	sky view factor (see Eq. 13)
F_2	horizon brightness coefficient [unitless]
F_ground	ground view factor (see Eq. 14)

3.3 Thermal Model

To simulate the operating temperature of the PV module based on ambient weather conditions and module mounting configuration, we use the cell temperature and module temperature model by Sandia National Laboratories [9]. First, the module back-surface temperature is calculated, based on irradiance, weather conditions, as well as the module construction and mounting type (Eq. 19).

$$T_\mathrm{m} = \mathrm{POA} \cdot \exp\left(a + b \cdot \mathrm{WS}\right) + T_\mathrm{a} \tag{19}$$

with

T_m	module back-surface temperature [°C]
a, b	parameters depending on module type and mounting configuration of the module (Tab. 3)
WS	wind speed [m/s]
T_a	ambient air temperature [°C]

Afterwards, the cell temperature is derived from the module back-surface temperature, the POA, and a temperature difference parameter (Eq. 20).

$$T_\mathrm{c} = T_\mathrm{m} + \frac{\mathrm{POA}}{1000\,\mathrm{W/m^2}} \cdot \Delta T \tag{20}$$

with

T_c	cell temperature [°C]
ΔT	temperature difference parameter [unitless]

Module Type	Mount	a	b
Glass/cell/glass	Open rack	−3.47	−0.0594
Glass/cell/glass	Close roof mount	−2.98	−0.0471
Glass/cell/polymer sheet	Open rack	−3.56	−0.0750
Glass/cell/polymer sheet	Insulated back	−2.81	−0.0455
Polymer/thin-film/steel	Open rack	−3.58	−0.113
22X Linear Concentrator	Tracker	−3.23	−0.130

Table 3: Values of parameters a and b of the Sandia module back-surface temperature model for common module types and configurations [9].

3.4 Incident Angle Modifier Model

The physical incident angle modifier (IAM) model is used to predict optical losses, like reflections, at the surface of a PV module based on the actual physical properties of the materials involved. The model described by Duffie and Beckman [6] is based on Snell's law in order to calculate the angle of refraction (Eq. 21). This is used along with Fresnel's and Bouguer's laws to calculate the radiation absorbed by a cell with

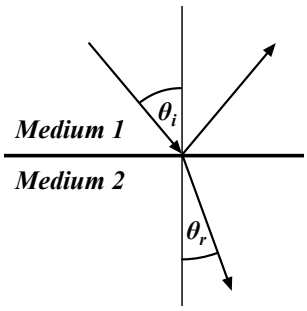

Figure 4: Angle of incidence θ_i and angle of refraction θ_r.

a glass cover (Eq. 22), which uses typical values for the glazing extinction coefficient and the glazing thickness. The incidence angle modifier itself is then the ratio of the transmittance for the angle of incidence and 0 ° (Eq. 23).

$$n_\mathrm{air} \cdot \sin\theta_\mathrm{i} = n_\mathrm{glass} \cdot \sin\theta_\mathrm{r} \Leftrightarrow \theta_\mathrm{r} = \arcsin\left(\frac{n_\mathrm{air}}{n_\mathrm{glass}} \cdot \sin\theta_\mathrm{i}\right) \tag{21}$$

$$\tau\alpha(\theta_\mathrm{i}) = \exp\left(-\frac{K \cdot L}{\cos\theta_\mathrm{r}}\right) \cdot \left[1 - \frac{1}{2} \cdot \left(\frac{\sin^2(\theta_\mathrm{r} - \theta_\mathrm{i})}{\sin^2(\theta_\mathrm{r} + \theta_\mathrm{i})} + \frac{\tan^2(\theta_\mathrm{r} - \theta_\mathrm{i})}{\tan^2(\theta_\mathrm{r} + \theta_\mathrm{i})}\right)\right] \tag{22}$$

$$K_{\tau\alpha}(\theta_\mathrm{i}) = \frac{\tau\alpha(\theta_\mathrm{i})}{\tau\alpha(0)} \tag{23}$$

with

n_air	refractive index of air ≈ 1
n_glass	refractive index of glass ≈ 1.526
θ_r	angle of refraction [°]
$\tau\alpha(\theta_\mathrm{i})$	transmittance-absorbtance product for incidence angle θ_i [unitless]
K	glazing extinction coefficient $\approx 4\,1/\mathrm{m}$ (for "water white" glass)
L	glazing thickness $\approx 2\,\mathrm{mm}$ (typical value)
$K_{\tau\alpha}$	incidence angle modifier [unitless]

The IAM is then used to calculate the effective irradiance. Therefore, we split the POA irradiance into its direct, sky diffuse, and ground diffuse components and multiply each of them with their IAM. The resulting sum is then the effective irradiance.

$$\mathrm{POA}_\mathrm{eff} = K_{\tau\alpha}(\theta_i) \cdot \mathrm{POA}_\mathrm{direct} + K_{\tau\alpha}(\theta_\mathrm{diffuse}) \cdot \mathrm{POA}_\mathrm{diffuse} + K_{\tau\alpha}(\theta_\mathrm{ground}) \cdot \mathrm{POA}_\mathrm{ground} \tag{24}$$

with

$\mathrm{POA}_\mathrm{eff}$	effective POA irradiance [$\mathrm{W/m^2}$]
$\mathrm{POA}_\mathrm{direct}$	direct component of POA irradiance [$\mathrm{W/m^2}$]
θ_diffuse	diffuse effective angle [°]
$\mathrm{POA}_\mathrm{diffuse}$	diffuse component of POA irradiance [$\mathrm{W/m^2}$]
θ_ground	ground effective angle [°]
$\mathrm{POA}_\mathrm{ground}$	ground component of POA irradiance [$\mathrm{W/m^2}$]

3.5 Photovoltaic Performance Model

The electrical power generated by a PV cell is typically modelled by the single diode model [5]. Its equivalent circuit (Fig. 5) treats the cell as a current source generating the light current, which is then distributed across a diode resembling the voltage-dependent current lost to recombination, the shunt resistance representing the current lost through leakage paths, and the series resistance representing the total internal resistance the current encounters as it travels through the PV cell components to the external terminals.

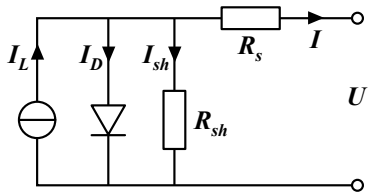

Figure 5: Equivalent circuit of the CEC six parameter PV module model.

After substituting the formulas for the diode current (Eq. 26) and shunt current (Eq. 27) into the formula for the output current (Eq. 25), we receive the formula of the CEC six-parameter PV module model by Dobos.

$$I = I_\mathrm{L} - I_\mathrm{D} - I_\mathrm{sh} \tag{25}$$

$$I_\mathrm{D} = I_0 \cdot \left[\exp\left(\frac{V + I \cdot R_\mathrm{s}}{a}\right) - 1\right] \tag{26}$$

$$I_\mathrm{sh} = \frac{V + I \cdot R_\mathrm{s}}{R_\mathrm{sh}} \tag{27}$$

with

I	output current [A]
I_L	light-generated current [A]
I_D	voltage-dependent current lost to recombination [A]
I_sh	shunt current [A]
I_0	diode reverse saturation current [A]
V	output voltage [V]
R_s	series resistance [Ω]
a	modified nonideality factor [V]
R_sh	shunt resistance [Ω]

Out of these six parameters, the light-generated current, the modified nonideality factor, and the diode reverse saturation current depend on weather conditions like temperature, air mass, and irradiance. Using their values measured at reference conditions, they can be adjusted to fit the current operating conditions (Eqs. 28 to 31).

$$\frac{a}{a_{\text{ref}}} = \frac{T_{\text{c}}}{T_{\text{NOCT}}} \tag{28}$$

$$I_L = \frac{\text{POA}_{\text{eff}}}{1000\,\text{W/m}^2} \cdot \frac{\text{AM}}{1.5} \cdot \left[I_{\text{L,ref}} + \alpha_{\text{sc,ref}} \cdot \left(1 - \frac{\text{Adjust}}{100} \right) \cdot (T_{\text{c}} - T_{\text{NOCT}}) \right] \tag{29}$$

$$\frac{I_0}{I_{0,\text{ref}}} = \left(\frac{T_{\text{c}}}{T_{\text{NOCT}}} \right)^3 \cdot \exp \left[\frac{1}{k} \cdot \left(\frac{E_{\text{g}}}{T} \bigg|_{T_{\text{NOCT}}} - \frac{E_{\text{g}}}{T} \bigg|_{T_{\text{c}}} \right) \right] \tag{30}$$

$$\frac{E_{\text{g}}}{E_{\text{g,ref}}} = 1 - 0.000\,267\,7 \cdot (T_{\text{c}} - T_{\text{NOCT}}) \tag{31}$$

with

a_{ref}	reference modified nonideality factor [V]
T_{NOCT}	nominal operating cell temperature [°C]
AM	air mass [unitless]
$I_{\text{L,ref}}$	reference light-generated current [A]
$\alpha_{\text{sc,ref}}$	reference temperature coefficient of short-circuit current [unitless]
Adjust	adjustment factor [unitless]
$I_{0,\text{ref}}$	reference diode saturation current [A]
k	Boltzmann constant $= 1.3807 \cdot 10^{-23}$ J/K
E_{g}	bandgap energy eV
$E_{\text{g,ref}}$	reference bandgap energy ≈ 1.121 eV (for silicon)

Now, we can solve the single diode equation under the current operating conditions. The solution space can be plotted, and the result is called the I-V curve of the module under those operating conditions. This I-V curve can then be used to determine the power output of the module. Since electrical power is the product of current and voltage, we can scan the curve for the maximum power point (MPP), the point where this product is greatest. This is our power output because, ideally, the maximum power point tracking (MPPT) controller of the inverter adjusts the voltage accordingly to keep the MPP.

3.6 Inverter Model

Using the Sandia Inverter Model [10], we can simulate the AC power output from the DC power input and DC voltage input. The model captures how inverter efficiency varies with both load and DC voltage, while also accounting for clipping and tare loss.

$$P_{\text{ac}} = \left(\frac{P_{\text{aco}}}{A - B} - C \cdot (A - B) \right) \cdot (P_{\text{dc}} - B) + C \cdot (P_{\text{dc}} - B)^2 \tag{32}$$

$$A = P_{\text{dco}} \cdot (1 + C_1 \cdot (V_{\text{dc}} - V_{\text{dco}})) \tag{33}$$

$$B = P_{\text{so}} \cdot (1 + C_2 \cdot (V_{\text{dc}} - V_{\text{dco}})) \tag{34}$$

$$C = C_0 \cdot (1 + C_3 \cdot (V_{\text{dc}} - V_{\text{dco}})) \tag{35}$$

with

P_{ac}	AC output power [W]
P_{aco}	AC power rating [W]
P_{dc}	DC input power [W]
P_{dco}	DC power input at reference voltage resulting in P_{aco} [W]
C_0	parameter defining the curvature of the relationship between AC power and DC power [unitless]
C_1, C_2, C_3	empirical parameters describing linear variations [1/V]

4 Optimization of the Module Orientation

The orientation of the PV modules plays a significant role in the resulting performance of the PV park. By adjusting the tilt and azimuth angles, the total incident solar radiation received by the PV modules can be influenced substantially throughout the year. To capture the most of the solar radiation energy, the solar rays must strike the modules perpendicularly. In order to find the optimal angles, the changing solar position throughout the day and the year, as well as weather conditions, must be taken into consideration.

4.1 Objective Function

The goal of this optimization is to find the pair of tilt and azimuth angles that maximizes the total solar incident on the module surface over one full year. The tilt angle is the angle between the module and the horizontal plane, and the range of its values is 0° to 90°. The azimuth angle is the compass direction the module faces, ranging from 0°, facing North, over 90°, facing East, and 180°, facing South, to 360°, facing North again. Based on the solar radiation input data from chapter 2.1 and the transposition model, as well as the solar position model from chapter 3, we can define our objective function as the maximum of the annual POA irradiance for any combination of tilt and azimuth angles.

4.2 Optimization Algorithm

Before finding the angle pair which maximizes the annual POA irradiance, an algorithm that calculates the annual POA irradiance for a given orientation and location must be created. Therefore, we combine the solar position model with a transposition model and solar radiation data. First, we gather the solar radiation data for the given location. Depending on the time resolution of the solar radiation data, we then calculate the solar position for each datapoint using the solar position model. Following, we can calculate each angle of incidence on the tilted plane. Next, we calculate the POA irradiance for each datapoint using the transposition model with the solar radiation data and the angle of incidence. Finally, we add up all of the POA irradiances. If the solar radiation data had datapoints for exactly one year, this sum is the annual POA irradiance. Otherwise, it must be normed to one year.

4.2.1 Unbounded Grid Search

The easiest way to find the pair of angles that yield the maximum annual POA irradiance is to try out each combination using an unbounded grid search. By calculating the annual POA irradiance for each tilt-azimuth angle combination, we make sure that we definitely find the global maximum. However, since the ranges of the tilt and azimuth angles are continuous, we must quantize them. In this thesis, we chose a step size of

1°. After calculating all the annual POA irradiances, we return the tilt and azimuth angles resulting in the highest annual POA irradiance.

4.2.2 Bounded Grid Search

A full grid search over 0° to 90° tilt and 0° to 360° azimuth covers a large search space where many combinations, such as those facing away from the equator or tilting vertically, yield suboptimal results. Therefore, we can bound the search by shrinking the ranges and exclude such combinations. This comes with the risk of missing a maximum that lies outside these bounds.

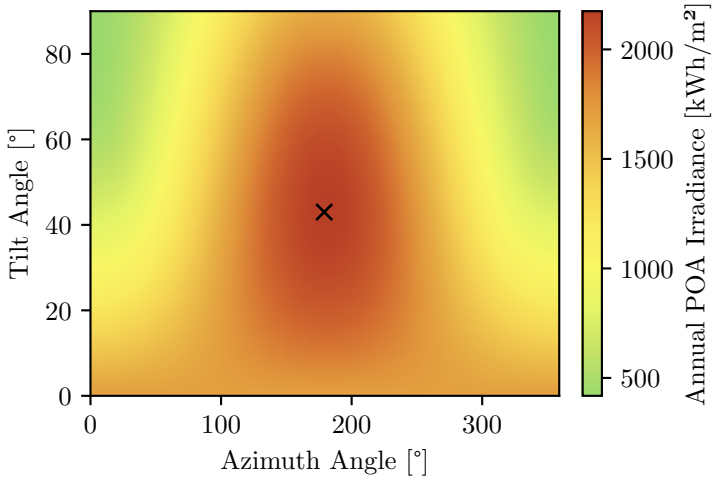

Figure 6: Annual POA irradiance heatmap as a function of tilt and azimuth at 48° N, 9.5° E, with the marker indicating the tilt-azimuth combination yielding maximum irradiance.

In Figure 6, you can see a heatmap showcasing the unbounded grid search for a location in Germany. It showcases the angle combinations that can be excluded, as previously discussed. Therefore, we chose to shrink the tilt angle range to 20° to 60° and the azimuth range to 135° to 225°. This reduces the number of combinations from 32 400 down to 3600. However, these bounds are chosen for Germany specifically and need to be adjusted for other locations on the globe, especially those in the southern hemisphere.

4.3 Results and Validation

In order to decide which transposition model and which irradiance data source to choose in the optimization, we compare their results to the optimal angles according to PVGIS' PV calculator [15]. The models' results are computed using pvlib python [2]. To make sure the results are consistent, we chose locations in Germany along the 9.5° E longitude line ranging from 47.5° N to 55° N in 0.5° steps. For each location, we calculate the optimal angles of our simulation with the ones of PVGIS' simulation. We

then calculate the Mean Absolute Error (MAE) between the two optimization results to compare the model composition and choose the best one of them.

4.3.1 Isotropic Sky Model with Clear Sky Model

Comparing the results from the isotropic sky model and the clear sky model to the optimal angles from PVGIS, you can see there is a substantial difference between them as shown in Figure 7. With a MAE of 3.375° for the optimal tilt and one of 4.9375° for the optimal azimuth angles, this combination of models is too inaccurate. It does not follow the general trends of the validation data from PVGIS. Where PVGIS' tilt angles decrease from latitudes 47.5° N to 49° N, the model's tilt angles increase from latitudes 47.5° N to 48.5° N. Furthermore, its azimuth angles are always either 180° or 179°, whereas the ones from the PVGIS validation set fluctuate between 172° and 180°. This is caused by the clear sky model not taking account of terrain shadows.

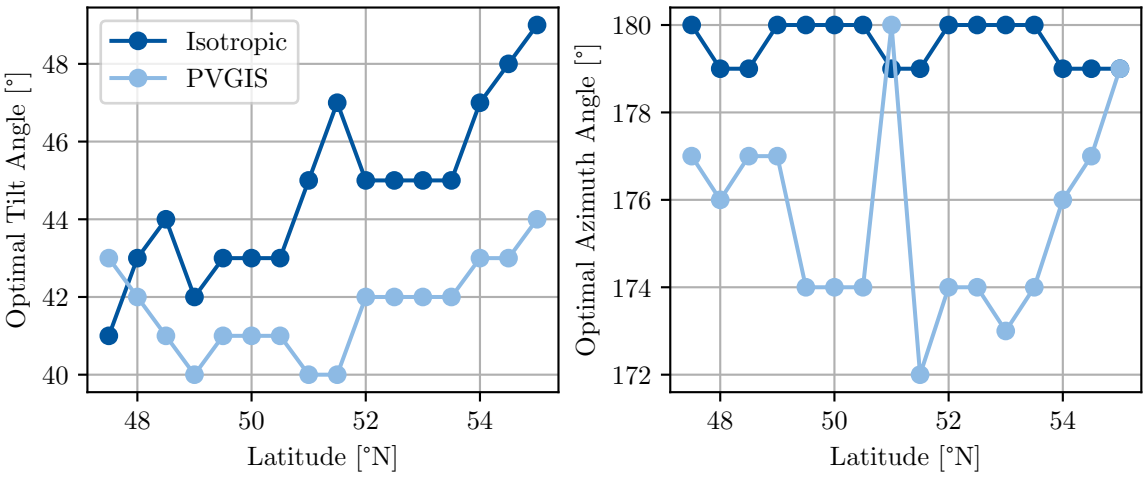

Figure 7: Comparison of simulated and PVGIS-derived annual optimal-tilt and azimuth angles along 9.5° E using the isotropic and clear sky models.

4.3.2 Isotropic Sky Model with PVGIS Irradiance Data

In order to improve the results of the isotropic sky model, we switch from the clear sky model to the hourly data from PVGIS-ERA5. Besides the obvious advantage that cloudy weather is taken into account now, this also has the benefit of including terrain shadows. As you can see in Figure 8, in comparison to the clear sky model, especially the optimal azimuth angles align much better with a MAE of 1.4375°. Whilst the MAE of the optimal tilt angles got a bit worse with 4.9375°, it now better resembles the trends of PVGIS' optimal tilt angles. However, it is conspicuous that the optimal tilt angles are solely lower than the ones from PVGIS, whereas the optimal azimuth angles are greater than or equal to PVGIS'.

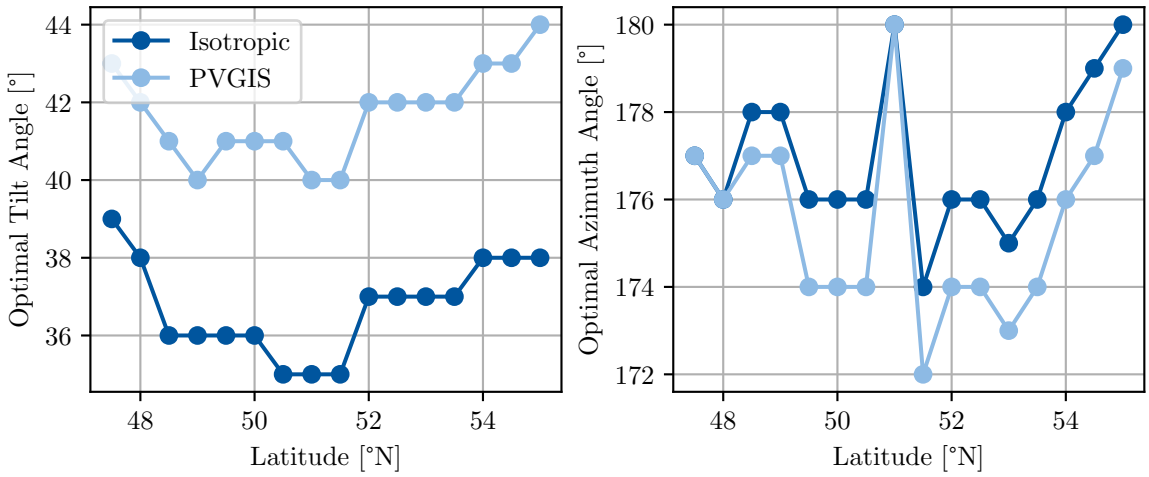

Figure 8: Comparison of simulated and PVGIS-derived annual optimal tilt and azimuth angles along 9.5° E, based on the isotropic sky model and PVGIS-ERA5 (2005-2023) weather data.

4.3.3 Perez Model with PVGIS Irradiance Data

To improve the results of the isotropic sky model, we switch to the more realistic Perez model and receive the results shown in Figure 9. This model has a MAE of 0.625° for the optimal tilt angle and 0.75° for the optimal azimuth angle. It also follows the trends of the angles from PVGIS with only slight differences and no outliers.

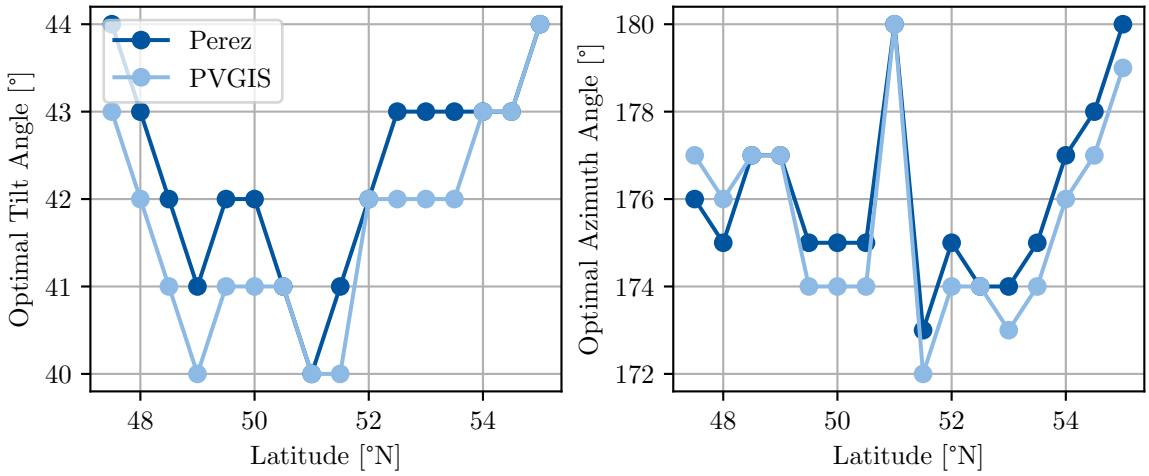

Figure 9: Comparison of simulated and PVGIS-derived annual optimal tilt and azimuth angles along 9.5° E, based on the Perez model and PVGIS-ERA5 (2005-2023) weather data.

4.3.4 Performance

In the previous comparisons, we ran the optimization using the unbounded grid search algorithm. However, we could also use the bounded grid search algorithm and still receive the same results, since we never left the specified bounds in any way.

In order to quantify the performance gains of the bounded grid search algorithm compared to the unbounded grid search algorithm, we performed a benchmark test of the previous three combinations of transposition models and irradiance data sources. Therefore, we chose the coordinates 48° N, 9.5° E and ran each simulation with the benchmarking tool hyperfine [14]. It calculates the mean execution time of a command over a series of ten runs. This mean execution time is then chosen as the runtime of the algorithm in the comparison (Table 4). The benchmarks were executed on an Apple Mac Studio with an Apple M1 Max (10-core CPU @ 3.23 GHz, 24-core GPU @ 1.30 GHz), 32 GiB unified memory, running macOS 15.6.1 (24G90), and Python 3.13.11.

Transposition Model	Irradiance Data Source	Unbounded Grid Search	Bounded Grid Search	Performance Gain
Isotropic Sky Model	Clear Sky Model	37.585 s	8.458 s	444.372 %
Isotropic Sky Model	PVGIS-ERA5	219.123 s	29.065 s	753.906 %
Perez Model	PVGIS-ERA5	928.982 s	100.283 s	926.360 %

Table 4: Time comparison results between the unbounded and bounded grid search algorithms.

The results of the benchmark show performance gains up to nine times faster, as expected, while still yielding the same optimization output. Although the performance gains of the bounded grid search algorithm for the isotropic sky model and clear sky model are not as significant as those for the isotropic sky model with PVGIS-ERA5 data or the Perez model with PVGIS-ERA5 data, they are still significant enough to recommend the bounded grid search algorithm over the unbounded one. Considering the overall performance of the models, we recommend using the Perez transposition model in conjunction with irradiance data from PVGIS-ERA5 and the bounded grid search algorithm.

5 Optimization of the Inter-Row Gap

In ground-mounted PV solar parks, the PV modules are typically arranged in rows. With the preceding optimization of the tilt and azimuth angles, we now know how to align a single row to collect the maximal irradiance throughout a whole year. When adding a second row, the question arises: how far the two rows should be placed apart? This distance between the panel rows is called the inter-row gap. Defining the optimum in this case is not as trivial as finding the optimal alignment. On the one hand, you want to minimize the gap in order to place as many panels as possible into the available area for the PV solar park. However, reducing the inter-row gap to zero, meaning having no gap at all, results in the anterior row casting a shadow onto the posterior row when the solar elevation angle is too low. This is called self-shading. So, on the other hand, you want to minimize the irradiance losses from self-shading, which means increasing the gap. In order to find the optimal balance between these two effects, we introduce a realistic model that simulates the losses caused by self-shading.

5.1 Self-Shading Model

In order to calculate the losses due to self-shading, we introduce a geometric model to calculate the shadow cast at each solar elevation angle. Therefore, we assume the Sun and the two PV module rows lie in the same plane, neglecting the difference between the Sun's azimuth angle and the PV module's azimuth angle. With the panel width, the tilt angle, and the inter-row gap, we can calculate the shallowest solar elevation angle at which no self-shading happens.

$$\alpha_{\text{full}} = \arccos \frac{h}{D} \tag{36}$$

$$h = w \cdot \sin \beta \tag{37}$$

with

α_{full}	shallowest solar elevation angle without self-shading [°]
h	height difference between the PV module's highest and lowest edges [m]
D	inter-row gap [m]
w	PV module's width [m]
β	PV modules's tilt angle [°]

If the solar elevation angle is shallower, the anterior PV module casts a shadow onto the posterior one. This causes a loss in energy yield of the posterior PV module. In this model, we assume a simplified half-cut PV module. Therefore, we split the PV module horizontally in half. When any part of a half is shaded, we assume that this half does not yield any energy anymore. This means, we can calculate another solar elevation angle which is the shallowest solar elevation angle at which the panel still yields 50 % of its energy. Any shallower solar elevation angle results in no energy yield.

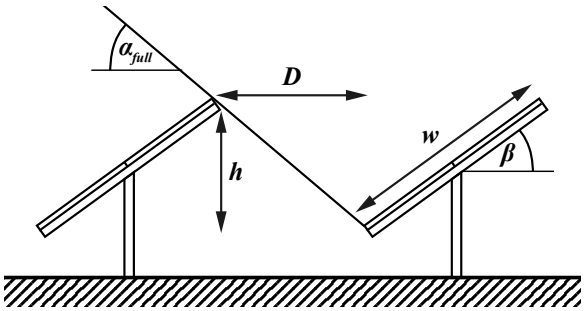

Figure 10: Geometric formulation to calculate α_{full}, the smallest solar elevation angle for which the anterior row's shadow misses the posterior row.

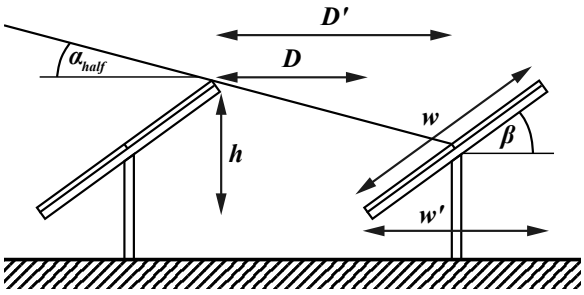

Figure 11: Geometric formulation to calculate the smallest solar elevation angle for which the anterior row's shadow misses the upper half of the posterior row's PV module.

$$\alpha_{\text{half}} = \arccos \frac{h}{2 \cdot D'} \tag{38}$$

$$D' = D + \frac{w'}{2} \tag{39}$$

$$w' = w \cdot \sin \beta \tag{40}$$

with

α_{half}	shallowest solar elevation angle with 50 % self-shading [°]
D'	inter-row gap to the middle of the posterior PV module row [m]
w'	PV module's projected width [m]

Depending on the solar elevation angle, we now have three different states of energy yield: when the solar elevation angle is steeper than or equal to α_{full}, the posterior PV module has no loss due to self-shading. When the solar elevation angle is steeper than or equal to α_{half} and shallower than α_{full}, the posterior PV module has 50 % loss due to self-shading. And lastly, when the solar elevation angle is shallower than α_{half}, the posterior PV module has 100 % loss due to self-shading. Note that the loss applies only to the direct POA irradiance, so even at 100 % loss the PV module could still

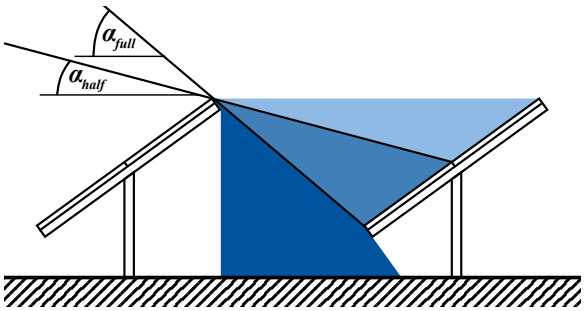

Figure 12: Visualization of the solar elevation angle intervals resulting in no (dark blue), half (mid blue) and full (light blue) self-shading.

yield power, but only from the, typically much lower, sky diffuse and ground diffuse POA irradiance components.

5.2 Objective Functions

Finding the optimal inter-row gap depends on the objective you want to optimize. Throughout this chapter, we focus on three objectives. First off, we want to find the optimal inter-row gap for the highest annual POA irradiance. In the next step, we want to simulate the AC power yield and optimize the inter-row gap for the highest annual AC power. Lastly, we introduce a cost model to calculate the levelized cost of energy (LCOE), which we will then use to find the optimal inter-row gap that minimizes the LCOE.

5.3 Optimizing after POA Irradiance

Since the self-shading model applies losses to the DNI of the irradiance data, we combine it with the transposition model. As for the transposition model and the irradiance data, we choose the Perez transposition model in conjunction with the PVGIS-SARAH3 hourly irradiance data set as in Chapter 4.3.3. This means for each data point of the PVGIS data set, we calculate the current solar elevation angle based on the solar position model. Depending on the tilt angle of the anterior PV module, we derive the loss factor for the direct POA irradiance from that solar elevation angle. After applying the Perez transposition model, this loss factor gets multiplied with the direct POA irradiance component. Summing up the shaded direct POA irradiance with the diffuse POA irradiance, we get the total shaded POA irradiance. After calculating this for each data point of the PVGIS data set, summing up the total shaded POA irradiances and norming them to one year, we get the annual shaded POA irradiance for that specific inter-row gap. Figure 13 shows how the inter-row gap and the caused self-shading affect the POA irradiance of the posterior PV module rows.

One might expect the graph of a smooth limited growth function, but instead, we observe the graph of a limited growth function with a kink at an inter-row gap between 77 cm and 84 cm. This can be explained when additionally the percentage of each loss

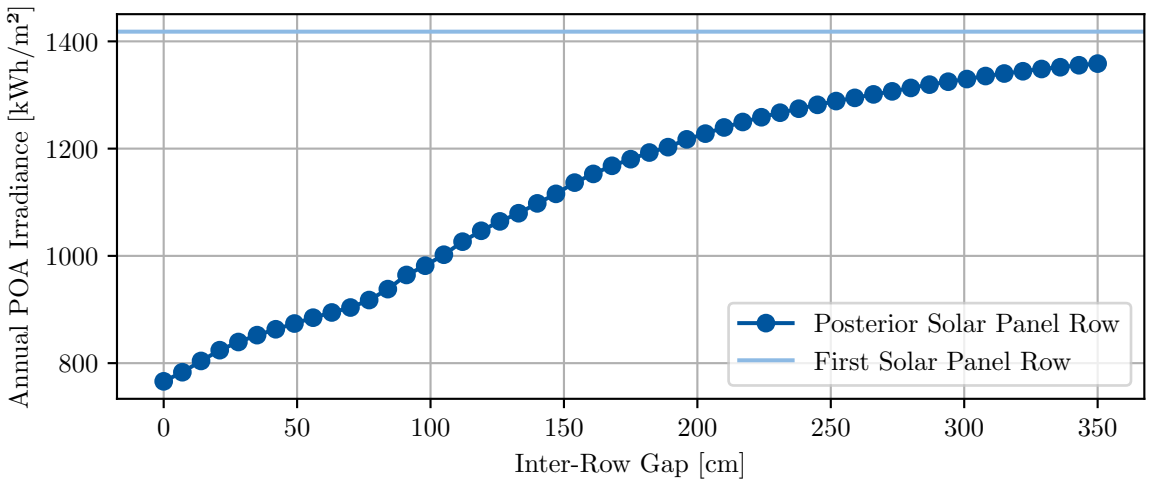

Figure 13: Impact of inter-row spacing on the annual POA irradiance received by the self-shaded posterior PV module in comparison to the anterior one at 50° N, 9.5° E.

is plotted for each inter-row gap as in Figure 14. Up to an inter-row gap of 77 cm, the posterior PV module is shaded at all times. This causes a loss of either 50 % or 100 %. Starting from 84 cm, the inter-row gap is big enough that no self-shading happens at times. Because the model uses this threshold system, there is an abrupt transition which causes the kink.

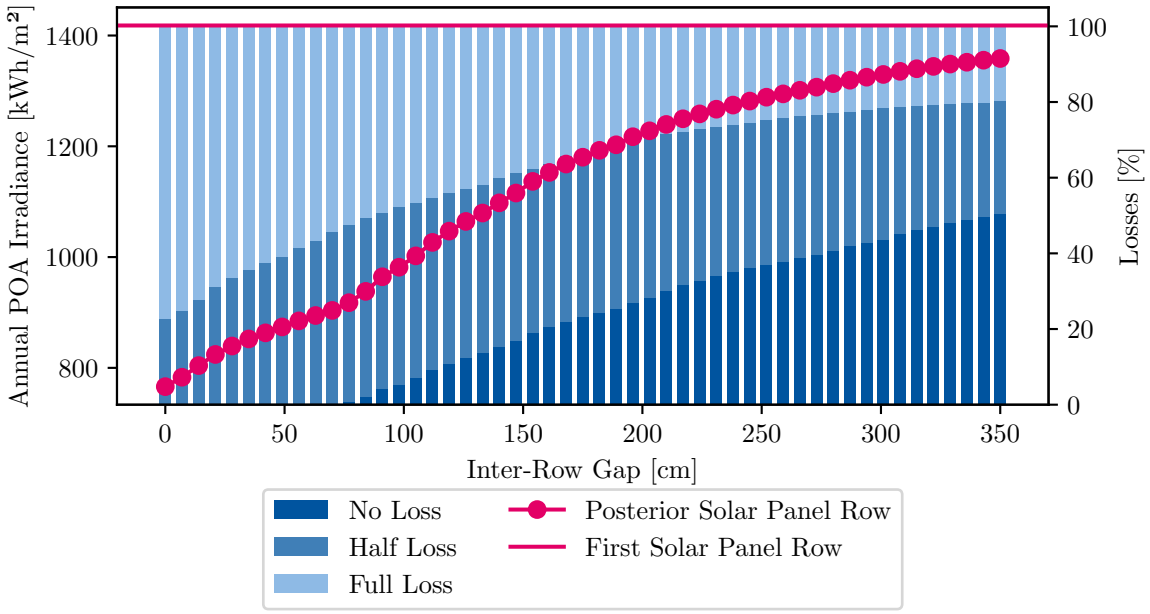

Figure 14: Proportions of losses applied to the direct POA irradiance component of the anterior PV module row for a range of inter-row gaps at 50° N, 9.5° E.

In order to find the optimal inter-row gap that maximizes the total annual POA

irradiance, we now require the available length of the area of the solar park measured perpendicularly to the orientation of the panel rows. This length must be bigger than two times the projected width of a PV module. Otherwise, the length is too short to fit two PV module rows; therefore, no inter-row gap exists. So, the minimum number of PV module rows is two since a second PV module row cannot result in less total annual POA irradiance even if it is shaded. The maximum number of PV module rows can be calculated by dividing the length by the projected PV module width.

$$N_{\max} = \lfloor \frac{l}{w'} \rfloor \tag{41}$$

with

$N_{\max}$ maximum number of PV module rows [unitless]
l length of the area of the solar park [m]

To calculate the inter-row gap for a given number of PV module rows which are spaced evenly across the available length, we use the following equation:

$$D_{\mathrm{N}} = \frac{l - N \cdot w'}{N - 1} \tag{42}$$

with

D_{N} inter-row gap for N PV module rows [m]
N number of solar panel rows [unitless]

To calculate the total annual POA irradiance, we sum up the annual POA irradiance without self-shading for the first row and N times the annual POA irradiance with self-shading for the respective inter-row gap:

$$\mathrm{POA}_{\mathrm{tot}} = \mathrm{POA}_{\mathrm{reg}} + N \cdot \mathrm{POA}_{\mathrm{shaded,D_N}} \tag{43}$$

with

$\mathrm{POA}_{\mathrm{tot}}$ total annual POA irradiance [W h]
$\mathrm{POA}_{\mathrm{reg}}$ unshaded annual POA irradiance [W h]
$\mathrm{POA}_{\mathrm{shaded,D_N}}$ annual POA irradiance with shading losses for inter-row gap D_N [W h]

Lastly, we compare the total annual POA irradiances for all N between $N_{\min}$ and $N_{\max}$.

The results of such a comparison are shown in Figure 15. There we used the dimensions of a typical PV module and the LR5-72HBD-550M panel by LONGi Green Energy Technology Co. Ltd. with a length of 2.278 m. For the area of the solar park, we chose a length of 30 m. As for the location, we chose 50° N, 9.5° E. The tilt angle of the panel has been determined by the simulation introduced in 4.3.3, which resulted in 42°. The results of this simulation suggest choosing as many PV module rows as you can fit into the area of the solar park. However, the gain in total POA irradiance gradually decreases.

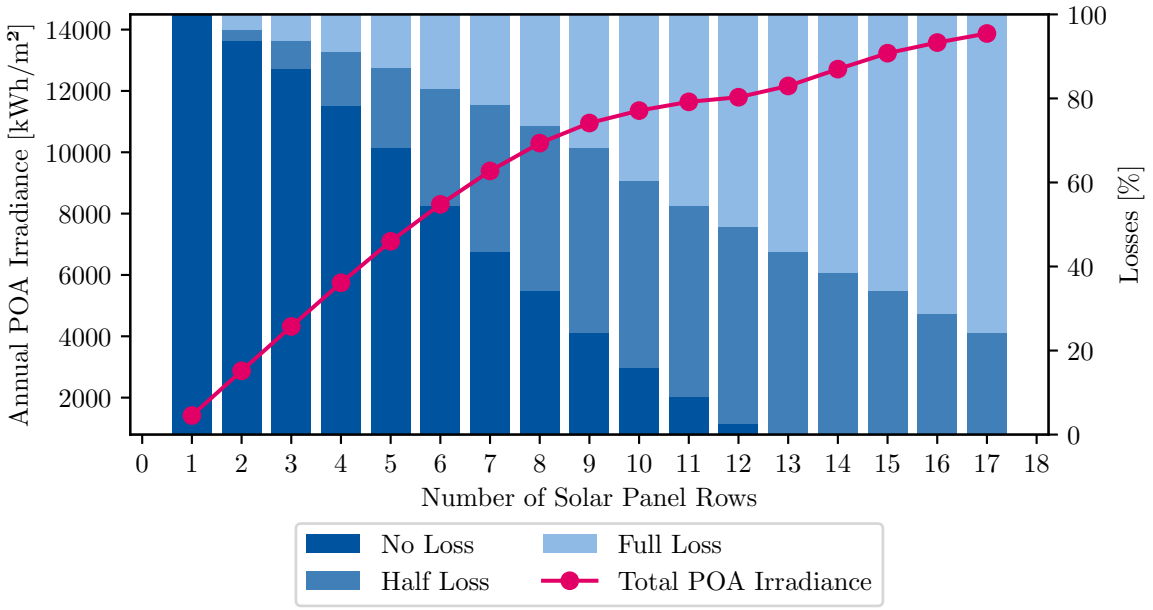

Figure 15: Total annual POA irradiance and proportions of self-shading losses, as a function of the number of panel rows accommodated within a 30 m long solar park at 50° N, 9.5° E.

5.4 Optimizing after Power Output

As an intermediary step, we reformulate the optimization objective to the power output of the solar park. In order to estimate the power output of a PV module, the POA irradiance is turned into DC and then AC power by using several simulation models. Using the IAM model introduced in Chapter 3.4, we calculate the effective irradiance on the tilted plane from the POA irradiance. Additionally, the Sandia thermal model (Chapter 3.3) is used to calculate the temperature of the cells. With these simulated values and the parameters of the CEC PV module database (Chapter 2.2.1), we can now use the CEC six-parameter PV module model introduced in Chapter 3.5 to simulate the DC power output. Combining this with the parameters of the CEC inverter database (Chapter 2.2.2), we use the Sandia Inverter Model introduced in Chapter 3.6 to simulate the AC power output. As discussed in Chapter 2.2, we picked a typical PV module (LONGi LR5-72HBD-550M) and inverter (ABB MICRO-0.25-I-OUTD-US-208 (208V)) from the CEC PV module and CEC inverter database. These picks are exemplarily and can be easily swapped out for other PV modules or inverters from any database providing the parameters listed in Chapter 2.2. As for the location, we choose again 50° N and 9.5° E, where the optimal tilt and azimuth angles are 42° and 175° based on our optimization from 4.3.3.

Since POA irradiance and AC output correlate, we get a similar result as with the optimization after maximum POA irradiance, as you can see in Figure 16. The optimal inter-row gap is the smallest, in order to fit the most panels into the available area length of the solar park.

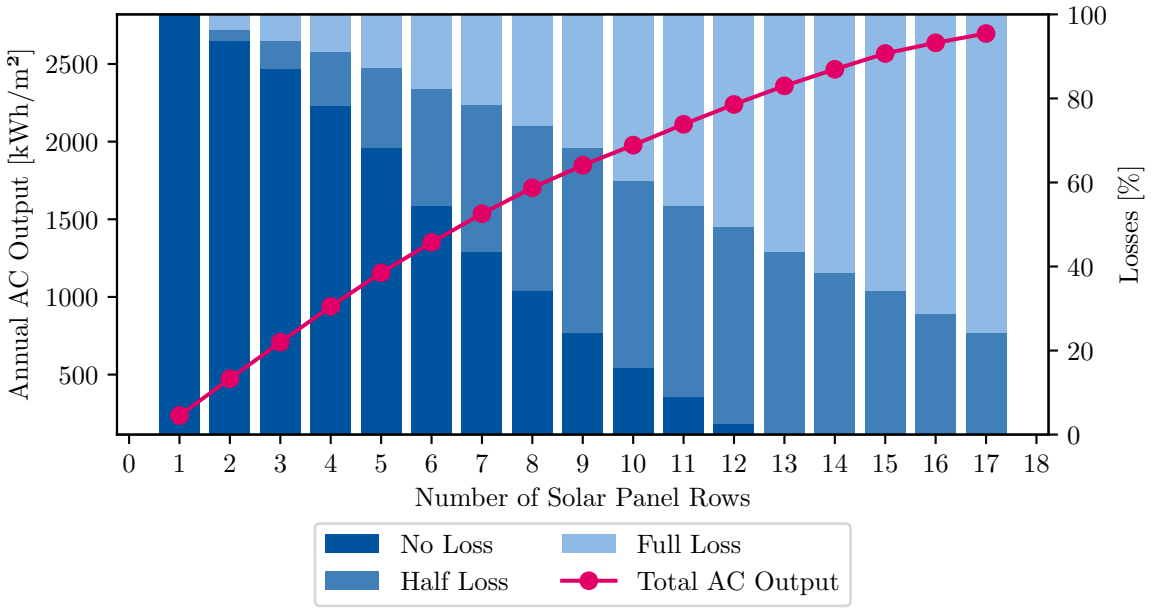

Figure 16: Total annual AC power and proportions of self-shading losses, as a function of the number of panel rows accommodated within a 30 m long solar park at 50° N, 9.5° E.

5.5 Optimizing after Levelized Cost of Electricity

The idea behind the optimization of LCOE is that while more PV module rows yield more power in total, they are also less efficient due to self-shading losses. Therefore, it is crucial to find the ideal tradeoff between energy production and component costs. As for the definition of the component costs, the NREL [18] divided the costs of a utility-scale PV system into the categories shown in Table 5. These costs are either dependent on the power production, such as the DC-rated capacity measured in $\$/\mathrm{kW_{dc}}$, the AC-rated capacity measured in $\$/\mathrm{kW_{ac}}$, and the capacity of the storage system in \$/kWh, or dependent on the size of the PV system, as for the area of the system measured in $\$/\mathrm{m^2}$.

Since we model a grid-connected solar park, we can omit the ESS cost. As for the DC-rated capacity, we retrieve the total maximum DC power our selected solar module can produce under standard test conditions from the CEC table. Once we know how many of those modules fit into a single row, we can calculate the total DC-rated capacity per PV module row. Using a typical DC/AC ratio of 1.2, we can calculate the required AC-rated capacity per PV module row by dividing the DC-rated capacity by the chosen DC/AC ratio. Now we can calculate the row-dependent cost like this:

$$\mathrm{cost_{row}} = (\mathrm{cost_{mod}} + \mathrm{cost_{ofc}} + \mathrm{cost_{oth}}) \cdot \mathrm{cap_{DC}} + (\mathrm{cost_{inv}} + \mathrm{cost_{EBOS}}) \cdot \mathrm{cap_{AC}}$$

In contrast to our algorithm to optimize the inter-row gap after power output, we now consider a square area instead of adding up the energy per square meter of each row.

Category	Cost
Utility Module Cost	372 $/kW$_{dc}$
Utility Inverter Cost	65 $/kW$_{ac}$
Utility Energy Storage System (ESS) Cost	323 $/kWh
Utility Structural Balance of System (SBOS) Cost	30 $/m^2
Utility Electrical Balance of System (EBOS) Cost	236 $/kW$_{ac}$
Utility Fieldwork Cost	61 $/m^2
Utility Officework Cost	66 $/kW$_{dc}$
Utility Other Cost	247 $/kW
Annual Utility Operations and Maintenance (O&M) Cost	16.58 $/a/kW$_{dc}$

Table 5: Utility-scale module, inverter, energy storage, SBOS, EBOS, office work, O&M, and other capital costs [18].

This means we also know the row-independent cost which, is calculated like this:

$$\text{cost}_{\text{area}} = (\text{cost}_{\text{SBOS}} + \text{cost}_{\text{fld}}) \cdot \text{area}$$

Like the previous algorithm for power output, we calculate the possible amounts of rows with their corresponding inter-row gaps. For each of these possible amounts of rows, we calculate the total capital expenditures (CAPEX) like this:

$$\text{cost}_{\text{CAPEX}} = \text{cost}_{\text{area}} + \text{cost}_{\text{row}} \cdot \text{N}$$

Besides CAPEX, there are also annual operational expenditures (OPEX) which can be calculated analogously using the O&M cost and the AC-rated capacity:

$$\text{cost}_{\text{OPEX}} = \text{cost}_{\text{O\&M}} \cdot \text{cap}_{\text{AC}} \cdot \text{N}$$

The resulting total expenditures (TOTEX) depend on the lifetime of the investment. We used a typical lifetime for utility-scale ground-mounted PV parks of 30 years.

$$\text{cost}_{\text{TOTEX}} = \text{cost}_{\text{CAPEX}} + \text{cost}_{\text{OPEX}} \cdot \text{LT}$$

With the annual AC output and a specified lifetime, which we set to 30 years, we can calculate the LCOE for each inter-row gap like this:

$$\text{LCOE} = \frac{\text{cost}_{\text{TOTEX}}}{\text{LT} \cdot P_{ac}}$$

When plotted, like in Figure 17, you receive a U-shaped curve for the LCOE values. The optimal inter-row gap is the one with the lowest corresponding LCOE value. In a study from July 2024, the Fraunhofer ISE [11] reported that large ground-mounted PV systems achieve LCOE values between 0.041 €/kWh and 0.050 €/kWh in southern Germany and 0.057 €/kWh to 0.069 €/kWh in northern Germany. Therewith, our simulation in southern Germany at 50° N, 9.5° E, which has an optimal inter-row gap at 1.4524 m and a LCOE of 0.0527 $/kWh, which are approximately 0.0448 €/kWh, fits in perfectly.

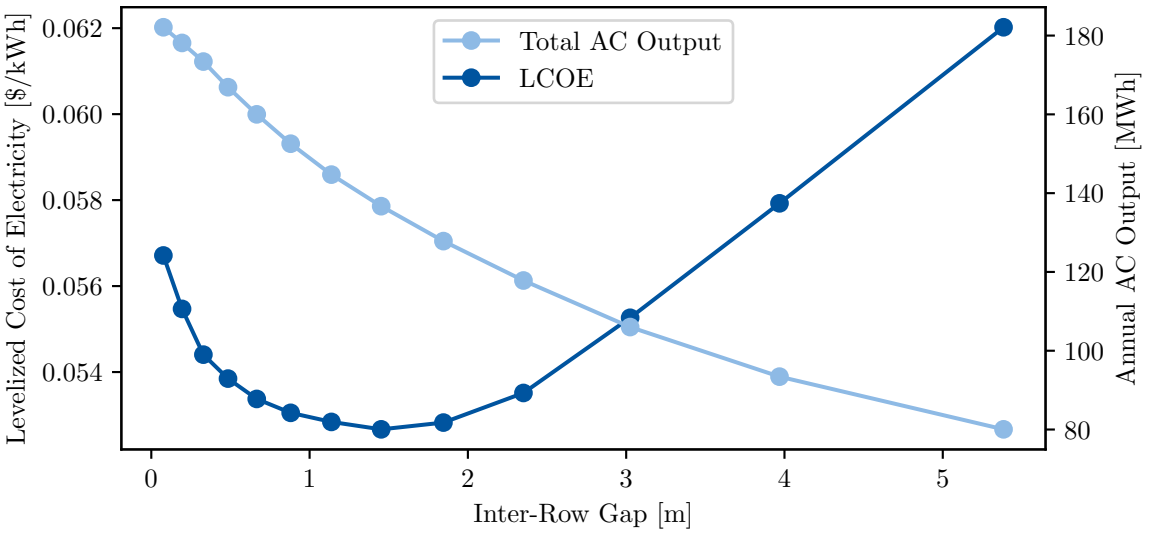

Figure 17: LCOE and total annual AC power, as a function of the size of the inter-row gap between PV module rows accommodated within a 30 m long and 30 m wide PV park at 50° N, 9.5° E.

5.6 Validation: Case Study Solarpark Langenenslingen-Wilflingen

To validate the optimization algorithm, we selected the Langenenslingen-Wilfingen solar park [1] in Germany as a benchmark case study. This facility was chosen due to its representative design parameters for ground-mounted PV installations in Germany and because it commenced operation in the current year, ensuring that configuration parameters, technology choices, and performance data reflect the latest module efficiencies and market cost structure relevant to today's LCOE optimization. To parameterize the validation case, the site's coordinates (48.123° N, 9.358° E) were used to derive the solar position and irradiance data, while the available land (60 ha of a 78 ha footprint) constrained feasible row counts and inter-row distances. The modules in use are the LONGi LR5-72HBD-550M units, whose parameters from the CEC PV module database were applied in the self-shading and PV performance models. The extrapolated annual energy production of 89.9 GW h was adopted as the operational reference for computing prediction error and validating the algorithm's LCOE-optimal inter-row gap.

After optimizing the orientation angles using our simulation introduced in chapter 4.3.3, we ran the self-shading model and calculated the optimal LCOE. As for the inputs of the models needed to compute the LCOE, we use the parameters of the LONGi LR5-72HBD-550M PV module and the ABB MICRO-0.25-I-OUTD-US-208 (208V) inverter. Additionally, we use the total available area of 60 ha to compute the width of the park. As for the shape of the park, we assume a quadratic area that is aligned to the optimal azimuth angle calculated in the first step. This means our park has a width of 774.597 m. The results of the optimization after LCOE are plotted in Figure 18. The optimization suggests an optimal inter-row gap of 1.555 m, yielding an

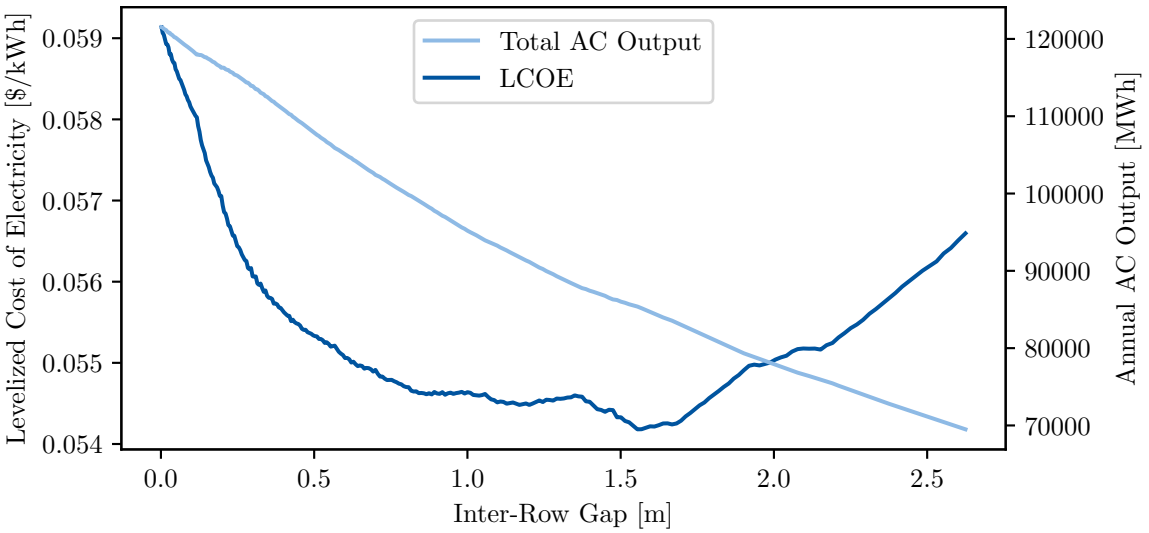

Figure 18: LCOE and total annual AC power, as a function of the size of the inter-row gap between PV module rows for the Solarpark Langenenslingen-Wilfingen at 48.123° N, 9.358° E.

annual AC output of 85.380 GW h at a LCOE of 0.054 $/kWh. This aligns with the extrapolated annual energy production of the park with an error of 5.028 %. Additionally, with an LCOE equivalent to 0.046 €/kWh, it lies in the boundaries for southern Germany of 0.041 €/kWh to 0.050 €/kWh as reported by the Fraunhofer ISE [11].

6 Conclusion

The objective of this paper was to develop an optimization framework for finding the best orientation and inter-row gap of a PV park. Therefore, we first introduced a selection of sources for irradiance data, as well as parameters for a typical PV module and an inverter. Next, we covered all relevant models necessary for simulating the performance of a PV park. Then, we proposed our two-step optimization framework, which consists of the optimization of the orientation as the first step and the optimization of the inter-row gap as a second step.

As for the optimization of the orientation, we optimized the tilt and azimuth angles of the fixed ground-mounted PV module after maximal annual POA irradiance. For this optimization, we compared two transposition models, the isotropic model and the Perez model, and two irradiance data source, a generative approach using the clear-sky model and the irradiance database PVGIS-ERA5. By comparing the results of the optimization with different underlying models to the optimal orientation suggested by PVGIS, we concluded that the Perez transposition model in conjunction with irradiance data from PVGIS-ERA5 was the most accurate. Additionally, we noticed that the runtime performance of that optimization can be significantly improved by adding location-dependent bounds to the grid-search algorithm. This sped up the optimization nine times, without sacrificing accuracy of the output.

Then we covered the second step of our optimization framework. Here we introduced a self-shading model which we used to simulate the effect of smaller inter-row gaps on the PV system's performance. Optimizing the inter-row gap was not as trivial as optimizing the orientation of the PV modules since with higher inter-row gaps the individual PV module rows produce more energy due to less self-shading, but you can fit less PV modules into the same area. This is why we chose to evolve our objective function from maximal annual POA irradiance, over maximal annual AC power output, to minimal LCOE. When optimizing after maximal annual POA irradiance and maximal annual AC power output, with increasing number of PV module rows the annual yield rises. This means, if you want to capture the most solar radiation or produce the most power choosing the smallest inter-row gap possible is optimal. However, this causes a large portion of the modules to be unproductive due to shading losses. In order to accomodote for this, we introduced a cost model which was then used to calculate the LCOE for each inter-row gap. In contrast to the previous objective functions, choosing the lowest inter-row gap did not result in the lowest LCOE due to the high TOTEX of the higher number of PV modules. Instead, the optimal inter-row gap with the lowest LCOE was always around 1.5 m at the locations we simulated. Increasing the gap further would increase the LCOE as well because the produced AC power would decrease faster than the decreasing TOTEX. A case study, where we compared our optimization results to the specifications of a modern PV park in Germany, showed that our optimization has small deviations but is quite accurate in general.

6.1 Future Work

Although this thesis provides a comprehensive analysis of optimizing the layout of PV parks, several aspects remain for future investigation.

First, you could optimize the orientation and inter-row gap based on different payment models. One could consider adapting the layout to maximize profit using the stock prices for electric energy. This could have the effect, that instead of south-facing azimuth angles, east- or west-facing azimuth angles are preferred. Since the demand for electrical energy is the highest during the morning and the evening, the lower solar energy yield during these hours could be compensated by higher feed-in revenues. Additionally, there might be feed-in tariffs during noon, because then typically the tendency is that more energy can be produced than consumed.

Furthermore, we only considered grid-connected, fixed ground-mounted PV modules. One could investigate whether single- or double-tracked modules are more profitable. The tracking ensures higher power yields, but comes with higher investment and maintenance costs. Similarly, electric storage systems could be used to aggregate electric energy during times where much power can be produced, but the demand on the power grid is low, in order to sell it during times where the demand is higher. However, these storage systems come with additional costs as well.

Lastly, we modelled the area of the PV park whose inter-row gap is to be optimized as a square with the equivalent area. However, this model is a simplification that can be improved. So instead of a square area, one could incorporate the real shape of the PV park, in order to provide more precise results.

References

[1] EnBW Energie Baden-Württemberg AG. Solarpark langenenslingen-wilflingen, 2025. URL https://www.enbw.com/unternehmen/themen/solarenergie/solarpark-langenenslingen-wilflingen/. Accessed: September 24, 2025.

[2] Kevin Anderson, Clifford Hansen, William Holmgren, Adam Jensen, Mark Mikofski, and Anton Driesse. pvlib python: 2023 project update. *Journal of Open Source Software*, 8(92):5994, December 2023. doi: 10.21105/joss.05994. URL https://doi.org/10.21105/joss.05994.

[3] Statistisches Bundesamt (Destatis). Korrektur: Stromerzeugung im 1. halbjahr 2025: 5,9 aus erneuerbaren energien, 2025. URL https://www.destatis.de/DE/Presse/Pressemitteilungen/2025/09/PD25_326_43312.html. Accessed: September 22, 2025.

[4] Statistisches Bundesamt (Destatis). Stromeinspeisung durch erneuerbare und konventionelle energieträger, 2025. URL https://www.destatis.de/DE/Presse/Pressemitteilungen/Grafiken/Energie/2025/_Interaktiv/20250908-stromeinspeisung-energietraeger.html. Accessed: September 22, 2025; Own visualization.

[5] Aron Dobos. An improved coefficient calculator for the california energy commission 6 parameter photovoltaic module model: Article no. 021011. *Journal of Solar Energy Engineering, Transactions of the ASME*, 134(2), 2012. ISSN 0199-6231. doi: 10.1115/1.4005759.

[6] J.A. Duffie and W.A. Beckman. *Radiation Transmission through Glazing: Absorbed Radiation*, chapter 5, pages 202–235. John Wiley & Sons, Ltd, 2013. ISBN 9781118671603. doi: https://doi.org/10.1002/9781118671603.ch5. URL https://onlinelibrary.wiley.com/doi/abs/10.1002/9781118671603.ch5.

[7] Pierre Ineichen and Richard Perez. A new airmass independent formulation for the linke turbidity coefficient. *Solar Energy*, 73(3):151–157, 2002. ISSN 0038-092X. doi: https://doi.org/10.1016/S0038-092X(02)00045-2. URL https://www.sciencedirect.com/science/article/pii/S0038092X02000452.

[8] Fritz Kasten and Andrew T. Young. Revised optical air mass tables and approximation formula. *Appl. Opt.*, 28(22):4735–4738, Nov 1989. doi: 10.1364/AO.28.004735. URL https://opg.optica.org/ao/abstract.cfm?URI=ao-28-22-4735.

[9] David L. King, William E. Boyson, and Jay A. Kratochvil. Photovoltaic array performance model. Technical Report SAND2004-3535, Sandia National Laboratories, Albuquerque, NM, 2004.

[10] David L. King, Sigifredo Gonzalez, Gary M. Galbraith, and William E. Boyson. Performance model for grid-connected photovoltaic inverters. Technical Report SAND2007-5036, Sandia National Laboratories, Albuquerque, NM, 2007.

[11] Christoph Kost, Paul Müller, Jael Sepúlveda Schweiger, Verena Fluri, and Jessica Thomsen. Study levelized cost of electricity - renewable energy technologies. Technical report, Fraunhofer Institute for Solar Energy Systems ISE, Freiburg, Germany, July 2024. URL https://www.ise.fraunhofer.de/content/dam/ise/en/documents/publications/studies/EN2024_ISE_Study_Levelized_Cost_of_Electricity_Renewable_Energy_Technologies.pdf.

[12] P.G. Loutzenhiser, H. Manz, C. Felsmann, P.A. Strachan, T. Frank, and G.M. Maxwell. Empirical validation of models to compute solar irradiance on inclined surfaces for building energy simulation. *Solar Energy*, 81(2):254–267, 2007. ISSN 0038-092X. doi: https://doi.org/10.1016/j.solener.2006.03.009. URL https://www.sciencedirect.com/science/article/pii/S0038092X06000879.

[13] National Renewable Energy Laboratory. System advisor model (sam), 2025. URL https://github.com/NREL/SAM. Accessed December 5, 2025.

[14] David Peter. hyperfine, March 2023. URL https://github.com/sharkdp/hyperfine.

[15] Photovoltaic Geographical Information System (PVGIS). Pvgis interactive tools, 2025. URL https://re.jrc.ec.europa.eu/pvg_tools/en/tools.html. Accessed: September 14, 2025.

[16] Photovoltaic Geographical Information System (PVGIS). Pvgis user manual, 2025. URL https://joint-research-centre.ec.europa.eu/photovoltaic-geographical-information-system-pvgis/getting-started-pvgis/pvgis-user-manual_en. Accessed: September 2, 2025.

[17] pvlib python. Pvlib user guide: Weather data, 2025. URL https://pvlib-python.readthedocs.io/en/stable/user_guide/modeling_topics/weather_data.html. Accessed: September 2, 2025.

[18] Vignesh Ramasamy, Jarett Zuboy, Michael Woodhouse, Eric O'Shaughnessy, David Feldman, Jal Desai, Andy Walker, Robert Margolis, and Paul Basore. U.s. solar photovoltaic system and energy storage cost benchmarks, with minimum sustainable price analysis: Q1 2023, 2023.

[19] Ibrahim Reda and Afshin Andreas. Solar position algorithm for solar radiation applications. *Solar Energy*, 76(5):577–589, 2004. ISSN 0038-092X. doi: https://doi.org/10.1016/j.solener.2003.12.003. URL https://www.sciencedirect.com/science/article/pii/S0038092X0300450X.

[20] Matthew Reno, Clifford Hansen, and Joshua Stein. Global horizontal irradiance clear sky models : implementation and analysis. Technical Report SAND2012-2389, Sandia National Laboratories, Albuquerque, NM, 2012.

[21] Viktor Wesselak and Sebastian Voswinckel. *Photovoltaik – Wie Sonne zu Strom wird*. Technik im Fokus. Springer-Verlag, Berlin, Heidelberg, 2 edition, 2016. ISBN 978-3-662-48905-5. doi: 10.1007/978-3-662-48906-2.